Weierstraß-Institut
für Angewandte Analysis und Stochastik
Leibniz-Institut im Forschungsverbund Berlin e. V.

Preprint ISSN 0946 – 8633

Impact of spatial inhomogeneities on on-axis pulse reconstruction in femtosecond filaments

Carsten Brée[1,2], Martin Kretschmar[3,4], Tamas Nagy[3,5], Heiko G. Kurz[3,4],

Uwe Morgner[3,4], Milutin Kovačev[3,4]

submitted: December 17, 2014

[1] Weierstrass Institute
Mohrenstr. 39
10117 Berlin, Germany
E-Mail: carsten.bree@wias-berlin.de

[2] Max Born Institute
Max-Born-Str. 2A
12489 Berlin

[3] Leibniz Universität Hannover
Welfengarten 1
30167 Hannover, Germany
E-Mail: kretschmar@iqo.uni-hannover.de
nagy@iqo.uni-hannover.de
kurz@iqo.uni-hannover.de
morgner@iqo-uni-hannover.de
kovacev@iqo.uni-hannover.de

[4] QUEST
Centre for Quantum Engineering and
Space-Time Research
Welfengarten 1
30167 Hannover, Germany

[5] Laser-Laboratorium Göttingen eV
Hans-Adolf-Krebs-Weg 1
37077 Göttingen, Germany

No. 2046
Berlin 2014

2010 *Mathematics Subject Classification.* Primary 78A60.

2010 *Physics and Astronomy Classification Scheme.* 42.65.-k, 42.65.Jx,42.65.Re,52.38.Hb.

Key words and phrases. Nonlinear Optics, All-optical Kerr effect, Pulse compression.

Financial support by the Deutsche Forschungsgemeinschaft (Grant KO 3798/3-1) is gratefully acknowledged.

Edited by
Weierstraß-Institut für Angewandte Analysis und Stochastik (WIAS)
Leibniz-Institut im Forschungsverbund Berlin e. V.
Mohrenstraße 39
10117 Berlin
Germany

Fax: +49 30 20372-303
E-Mail: preprint@wias-berlin.de
World Wide Web: http://www.wias-berlin.de/

Abstract

We demonstrate a strong influence of the spatial beam profile on the vacuum-propagated on-axis pulse shapes for a femtosecond filament in argon. The effects can be minimized by transmitting the filament into the far-field by a laser-drilled pinhole setup. Using this method, we can monitor the pulse compression dynamics along the entire longitudinal extension of the filament, including the ionization-induced plasma channel.

1 Introduction

Femtosecond filamentation provides a rich testing environment in the field of extreme nonlinear optics [1, 2]. Owing to the extreme light intensities, which can approach the order of inner atomic field strengths, a filament leads to a self-induced, transient refractive index in the propagation medium, eventually leading to beam self-guiding due to a delicate balance of focusing and defocusing nonlinearities [3]. In addition, the interplay of transient nonlinearities strongly affects the on-axis temporal pulse profile [4, 5], and it has been experimentally demonstrated that pulses undergoing filamentary propagation have the capability of temporal self-compression into the few-cycle domain [6]. In this respect, recent controversies on the current theoretical model of filamentation led to an increasing interest in accurately monitoring the filamentary pulse and plasma density evolution along the filament axis [7, 8, 9, 10, 11]. This gives the possibility to test the recent predicitions on the existence of nearly plasmaless filaments [12] maintained by a higher-order, saturable Kerr nonlinearity. Furthermore, the dynamics of temporal self-compression is quite different in the current model compared to high-order Kerr models [10], which strongly fostered scientific efforts to devise methods allowing for an in-situ measurement of the evolution of (spatio)temporal pulse shapes in the filament. In fact, a promising progress in this direction has recently been achieved in Ref. [13] which demonstrated a direct reconstruction of filamentary pulses using the transient-grating cross-correlation FROG technique. However, due to the high intensities involved, most other approaches employ indirect measuring methods, which rely on coupling the beam out of the filament, an appropriate attenuation of the beam and a subsequent propagation stage towards the pulse diagnostics, typically SPIDER [14] or second harmonic FROG [15]. In early experiments, the filament was ignited in a pressurized gas cell, with laser pulses entering and leaving the cell through sufficiently thin silica windows. However, nonlinear and dispersive effects inside the exit window have a quite dramatic impact on the pulse shape [16]. Although it has been demonstrated that the pulse can restore its original temporal shape [17], this only happens under suitable experimental conditions [18]. Furthermore, due to ionization induced damage, only pulses in the lower intensity, postionization regime [19] of the filament can be coupled out through the exit window. Therefore, for experimental setups which employ silica windows for coupling the pulse into and out of the gas cell, the plasma-dominated propagation regime in the vicinity of the nonlinear focus is

not accessible for pulse diagnostics. In order to circumvent these problems, the silica window was replaced in Ref. [11] by a so-called aerodynamic window. Alternatively, the pulse evolution was recently successfully monitored by coupling the pulse out into the vacuum through a self-induced pinhole, and by employing a suitable translation stage to scan along the longitudinal filament axis [20]. In this work, the evolution of the on-axis temporal pulse shape along the filament axis was measured. The dynamics of temporal self-compression was observed in good agreement with theoretical predictions. But also in these refined setups, the pulse still undergoes a certain propagation towards the diagnostics after being outcoupled. Since filamentary self-compression is based on a dynamical interplay of self-focusing and defocusing, these nonlinear effects unfortunately lead to a spatiotemporally imhomogeneous intensity distribution within the pulsed beam. Especially, filamentary pulse self-compression has been demonstrated to occur only at on-axis position[21], while off-axis pulse components, i.e. the so-called photon bath or reservoir, are unaffected by temporal self-compression. Hence, there is a resulting necessity to spatially confine the beam to the on-axis component for the reconstruction of the pulse shape. This can be realized by using suitable apertures or by truncating the beam by employing a laser-drilled pinhole, as done in our previous work. The latter method is advantageous since it enables a truncation and pulse reconstruction of the filament directly within the plasma-driven channel. However, since in most setups the beam propagates into the far field before reaching the pulse diagnostics, the diameter of the pinhole has a crucial impact on the measured pulse shapes in the far field.

In the current manuscript, we therefore investigate this crucial dependence of the reconstructed pulse shapes on the selected on-axis portion of the beam. We demonstrate that this is a consequence of the strongly inhomogeneous spatiotemporal intensity distribution. We furthermore show that a sufficiently small pinhole or aperture maps the filamentary on-axis pulse shape at the pinhole nearly undisturbed into the far field. This fact was exploited in our recent work [20], and here we provide additional theoretical investigation of the impact of these effects.

2 Theoretical models of near and far-field evolution

Our numerical model of filamentary propagation is based on the forward Maxwell equation with eliminated THG term [22]. In the frequency domain, it reads as

$$\partial_z \widehat{\mathcal{E}}(r,z,\omega) = \frac{i}{2k(\omega)}\nabla_\perp^2 \widehat{\mathcal{E}}(r,z,\omega) + i(k(\omega) - \frac{\omega}{v_g})\widehat{\mathcal{E}}(r,z,\omega) + \frac{i\mu_0\omega^2}{2k(\omega)}\left(\widehat{P}_{\mathrm{NL}} + i\frac{\widehat{J}}{\omega}\right). \quad (1)$$

Here, $\widehat{\mathcal{E}}(r,z,\omega)$ is the positive frequency part of the Fourier transform of the real electric field $\mathcal{E}$ (analytic signal), and it is assumed that a cylindrical symmetry of the beam around the optical axis is maintained during propagation. The parameter r denotes the transverse radial coordinate in the diffraction plane, and z denotes the longitudinal distance along the filament axis. The gas dispersion is modelled by the frequency dependence of the wave number $k(\omega)$ according to Ref. [23]. The simulations were performed in a reference frame comoving with the group velocity v_g of the pulse. The nonlinear polarization density P_{NL} reads in the time domain as

$$P_{\mathrm{NL}} = \frac{3}{8}\epsilon_0\chi^{(3)}|\mathcal{E}(r,z,t)|^2\mathcal{E}(r,z,t). \quad (2)$$

The charge current density J due to self-induced ionization effects is governed by the Drude model for a homogeneous, uncorrelated plasma of density $\rho(r,z,t)$. The latter is governed by

the rate equation

$$\partial_t \rho(r,z,t) = w(I)(\rho_0 - \rho) + \frac{\sigma(\omega_0)}{I_p}\rho I. \tag{3}$$

The ionization rate $w(I)$ depending on the light intensity I is modelled according to Ref. [24] and accurately describes strong field ionization effects in the multiphoton, tunneling and intermediate regime. Here, $\rho_0 = 2.7 \times 10^{25}\mathrm{m}^{-3}$ denotes the neutral gas density, $\sigma(\omega_0) = 1 \times 10^{-19}\mathrm{cm}^2$ denotes the cross section for collisional ionization in the vicinity of the carrier frequency ω_0, and $I_p = 15.76\,\mathrm{eV}$ denotes the ionization potential of argon. To analyze the propagation into the far field after the pulse is coupled out of the filament, we subsequently solve the Fraunhofer diffraction integral. For a radially symmetric electric field distribution, it is given by the Fourier-Hankel transform

$$\widehat{\mathcal{E}}_{\mathrm{ff}}(k_\perp,\omega) = 2\pi \int_0^{d/2} r' dr' \widehat{\mathcal{E}}_{\mathrm{nf}}(r',\omega,z) J_0(k_\perp r') \tag{4}$$

Here $\mathcal{E}_{\mathrm{ff}}$ is the electric field distribution in the transverse detector plane in the far field, while $\mathcal{E}_{\mathrm{nf}}$ is the field distribution in the near field, directly within the filament. In the far field, the transverse spatial frequency $k_\perp$ is related to the diffraction angle according to $k_\perp = k\sin\theta \approx k\theta$, and $k = 2\pi/\lambda$ is the wavenumber. The integration is performed over the radius of the pinhole, whose diameter is given by d. From Eq. (4), the far field spatio-spectral distribution in the detection plane can then be obtained from $\theta \approx r/z_{vac}$, where r is the transverse radius in the far field diffraction plane. Given the applicability of the far field approximation, the distance z_{vac} between the detector and the pinhole only determines the radial scale of the diffraction pattern in the detection plane. In our experiment, the pinhole diameter d is of the order of some 100 microns, and $z_{vac} = 1.75\,\mathrm{m}$. For a center wavelength of $\lambda = 800\,\mathrm{nm}$, this indeed ensures the validity of the far field approximation, since $d^2/(\lambda z_{vac}) \ll 1$ for the parameters employed. The transverse radius in the diffraction plane of the filament (in the near field) is denoted r' and z denotes the longitudinal position along the filament axis, i.e., according to Ref. [20], the position of the pinhole relative to the position of the curved mirror which focuses the laser beam into the gas cell.

3 Numerical results

We solve Eq. (1) for a Gaussian input beam with a beamwaist of $w_0 = 0.9\,\mathrm{cm}$, a focal length of $f = 200\,\mathrm{cm}$, a pulse duration of $t_p = 45\,\mathrm{fs}$ and a carrier frequency of $\nu = 385\,\mathrm{THz}$. The input pulse energy was adapted to the experimental conditions of $0.9\,\mathrm{mJ}$ [20]. Since clipping the input profile with a diaphragm avoids beam instabilities and multifilamentation, we further modulated the input spatial profile with an $N = 16$ supergaussian to represent a diaphragm of $0.7\,\mathrm{mm}$ diameter. With these initial conditions, the evolution of the temporal on-axis profile in the filament is as shown in Fig. 1**a**. The pulse undergoes the well-known pulse splitting and focusing-defocusing dynamics in the vicinity of the nonlinear focus, which in the postionization regime leads to a refocused, sub-$5\,\mathrm{fs}$ FWHM few-cycle structure in the trailing part and a small leading sub-pulse. The generated self-compressed pulse propagates stable for approximately $20\,\mathrm{cm}$. Figure 1**b** shows the corresponding evolution if the pulses are allowed to propagate into the far field, without any appropriate selection of the filament core using a pinhole. Since here the unclipped beam propagates into the far field, $d = \infty$ has been applied in Eq. (4).

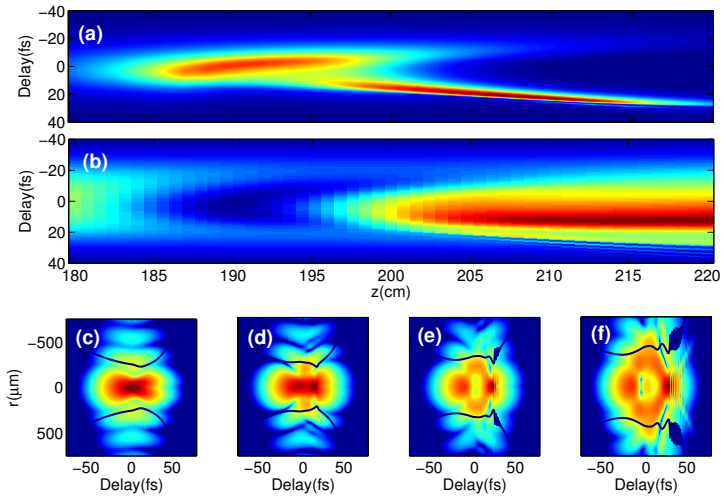

Figure 1: (color online) **a** Evolution of near field temporal intensity profile in the filament. **b** Corresponding evolution after propagation into the far field. **c**-**f** Spatiotemporal intensity distribution in the near field at $z = 190, 200, 210$ and 220 cm. Dark blue solid lines correspond to instantaneous spatial RMS radius of the beam.

The on-axis temporal profiles in the detection plane are obtained by letting $k_\perp = 0$ and performing the Fourier transform back into the time domain. As Fig. 1**b** reveals, vacuum propagation towards the detector strongly affects the measured pulse profiles. In fact, no trace of pulse self-compression is left, and considerably longer pulses are measured at the detector. To analyze

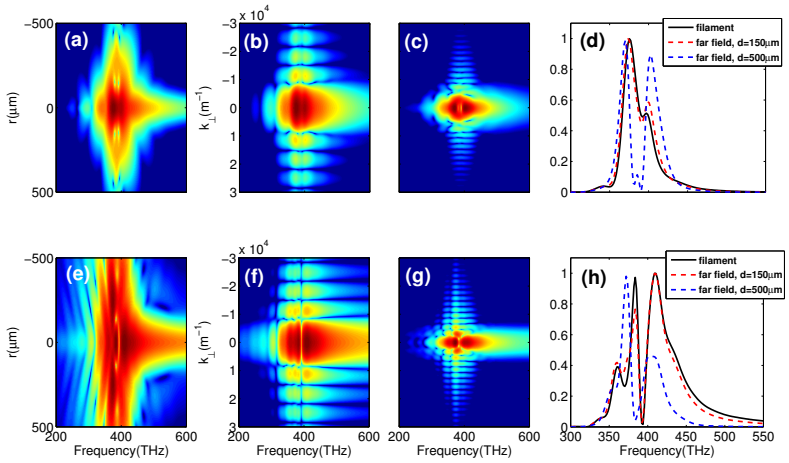

Figure 2: **a** Near field spatio-spectral intensity distribution at $z = 200$ cm. **b** Corresponding far field spectrum (Fourier-Hankel transform) after transmission through a $d = 150\,\mu$m pinhole **c** Correspondingly, for a $d = 500\,\mu$m pinhole **d** Near field on-axis spectrum (black solid line), far field on-axis spectrum for $d = 150\,\mu$m (red dashed line), far field on-axis spectrum for $d = 500\,\mu$m (blue dashed line). **e**-**h** Same as **a**-**d**, but for the filament pulse at $z = 220$ cm.

the origins of this effect, in Figs. 1**c**-**f**, we elucidate the involved spatiotemporal structure of the filament beam at $z = 190, 200, 210$ and 220 cm propagation distance. As the dark blue lines reveal, the RMS radius of the beam strongly varies with temporal delay. If these pulses were

coupled out of the filament without appropriate selection of an on-axis portion using a pinhole or diaphragm, subsequent vacuum propagation would strongly affect the on-axis temporal pulse shape, even in the absence of gas dispersion. This is a direct consequence of the fact that each temporal slice of the beam has its individual diffraction length according to $z_R(t) = \pi w_0^2(t)/\lambda$, where $w_0(t)$ is the beamwaist of the respective temporal slice at delay t, cf. Figs. 1**c**-**f**. The delay-dependent diffraction length, in addition with the aquired spatial phase curvature which may also strongly vary with delay, have a strong impact on the vacuum propagation into the far field. However, the impact of vacuum propagation on the pulse shapes can be considerably reduced by transmitting the beam through a pinhole before it propagates into the farfield, as will be demonstrated in the following. The inhomogeneity of the spatiotemporal intensity distribution, which strongly affects the measured pulse shapes in the far field, is also reflected in the spectral domain. This is shown in Fig. 2**a**, which depicts the spatio-spectral intensity distribution within the filament at $z = 200$ cm. However, for a sufficiently small pinhole with $d = 150\mu$ m for coupling the beam out into the vacuum, the on-axis spectrum can be transmitted into the far field nearly undisturbed, as revealed by Fig. 2**b**, which shows the far field spectrum in the $(k_\perp, \omega)$ domain. Besides the characteristic sidelobes generated at higher spatial frequencies due to transmission through the pinhole, we observe that the on-axis components close to $k_\perp = 0$ reproduce the on-axis spatio-spectral distribution directly in the filament. In contrast, the correspondence of near and far-field spectra is strongly deteriorated for a larger pinhole diameter of $d = 500\,\mu$m as depicted in Fig. 2**c**. This also becomes clear by comparing on-axis spectra in the filament (black solid line), and in the far field, cf. Fig. 2**d**. While the far-field on-axis spectrum is a nearly unchanged reproduction of the on-axis filament spectrum for the smaller pinhole (green dashed line), the far field on-axis spectrum corresponding to the larger pinhole strongly deviates from the near field on-axis spectrum. Especially, the far field spectrum has a pronounced mininum at the carrier frequency of $\nu = 385$ THz, which is related to the fact that frequency components close to the carrier frequency exhibit a stronger transverse localization (cf. Fig. 2a) and therefore diffract more rapidly. Similarly, Figs. 2**e**-**h** depict near and far-field spectra for the filament pulse coupled out at $z = 220$ cm. Again, for the smaller pinhole diameter, the on-axis spectrum is reproduced in the far field with good accuracy, while for the larger pinhole diameter, the on-axis far-field spectrum strongly deviates. In the latter case, we also find a significant reduction of the on-axis spectral bandwidth at the detector for the large pinhole diameter. Therefore, we find that the spectral shape in the far field is strongly sensitive to the employed pinhole diameter, leading to an equally dramatic effect in the time domain.

Evaluating Eq. (4) for $k_\perp = 0$ and Fourier transforming back into the time domain, we obtain the on-axis temporal pulse shape in the far field. For a pinhole diameter of $d = 500\,\mu$m, the evolution of the on-axis temporal intensity profile detected in the far field is depicted in Fig. 3**a**. It corresponds to the near-field evolution shown in Fig. 1a. The pulses in the detection plane are considerably longer than the near field pulse profiles, and it is obvious that a pinhole diameter of $500\,\mu$m is still too large to reveal the actual self-compression dynamics and the generation of few-cycle pulses. Therefore, the pinhole diameter has to be further decreased in order to truncate the photon bath and select the filament core only. Indeed, for $d = 150\,\mu$m, (cf. Fig. 3**b**), the near field pulse evolution is reproduced in the far field, and reveals the characteristic pulse splitting and the refocusing of a trailing portion of the pulse which is further compressed into the few-cycle regime. For $d = 150\,\mu$m, the temporal profiles of the near field pulses in the postionization regime $z > 200$ cm appear only slightly longer after transmission into the far-field and maintain their few-cycle characteristics, as shown by the light dashed line in Fig. 3**c**, which shows the FWHM duration versus propagation distances of the measured and simulated

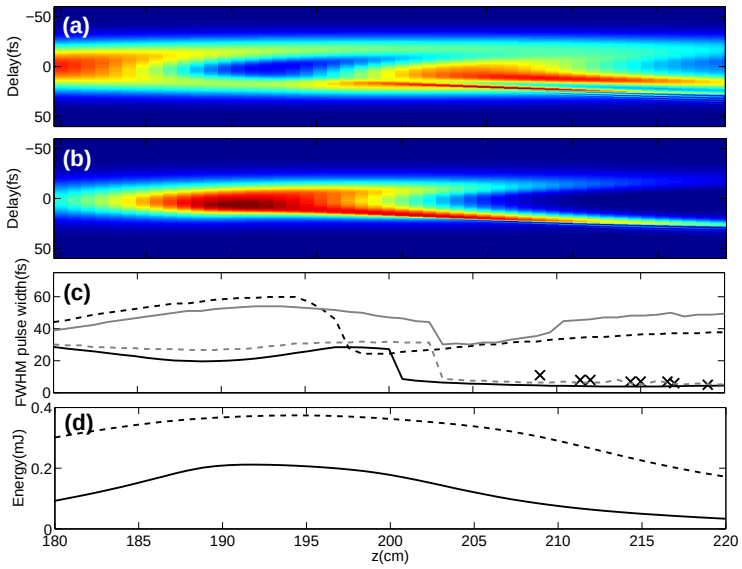

Figure 3: Evolution of temporal intensity profile in the far field for **a** $d = 500\,\mu$m pinhole and for **b** $d = 150\,\mu$m pinhole. **c** Evolution of FWHM pulse duration versus propagation distance for the near-field (dark solid line), and the far-field for a $d = \infty$ (dark dashed line), $d = 500\,\mu$m (light solid line), and $d = 150\,\mu$m (light dashed line). Crosses indicate experimentally measured pulse durations. **d** Energy transmitted through pinhole versus z. Dashed line: pinhole diameter $d = 500\,\mu$m, Solid line: $d = 150\,\mu$m.

pulses. The shortest attainable pulse duration in the near-field is $t_p \approx 4$ fs. For the small pinhole $d = 150\,\mu$m, this value only slightly increases to 5 fs, while both for the $d = 500\,\mu$m and the $d = \infty$ pinholes, the obtained pulse durations are no shorter than 20 fs. Since our results clearly show that filamentary self-compression is only effective at an on-axis position of the filament, it is subject to a trade-off between the pulse duration in the far field and the conversion efficiency. This is illustrated in Fig. 3**d**, which shows the transmitted energy versus propagation distance in the filament for two different pinhole diameters. For the larger pinhole diameter of $d = 500\,\mu$m, the shortest pulse duration of $\tau \approx 30$ fs is obtained at $z = 203.2$ cm. In this case, the energy transmitted through the pinhole is 0.35 mJ, i.e. a conversion efficiency of 38%. A considerably shorter pulse with a duration of 4 fs can be extracted at $z = 219$ cm for the smaller pinhole with $d = 150\,\mu$m. However, in this case the conversion efficiency drops down to 3.8%, with a transmitted energy of 0.035 mJ.

4 Experimental results

In order to further demonstrate the advantages of truncating the filament through pinholes, we also present additional experimental evidence obtained with the experimenal setup of Ref. [20]. Here, a 35 fs, 0.9 mJ beam is focused (f=2m) into a semi-infinite gas-cell to ignite a filament in 1 bar of argon. The high-intensity pulse propagates until its nonlinear propagation is stopped by a differential pumping stage with two laser-drilled pinholes. Subsequently, the pulse propagates under vacuum conditions for 1.75 m into the far-field, where it is analyzed by an all-vacuum SHG-FROG setup [15]. The measured pulse durations along z is indicated by the crosses in Fig. 3**c**.

The evolution of the temporal profile along the filament axis is shown in Fig. 4 and reveals several features also found in the simulations. First, the characteristic pulse splitting dynamics can be clearly observed. Second, the trailing pulse at positive delays is further compressed with increasing propagation distance, cf. the crosses in Fig. 3**c**, which shows the FWHM duration versus propagation distance of the measured and simulated pulses.

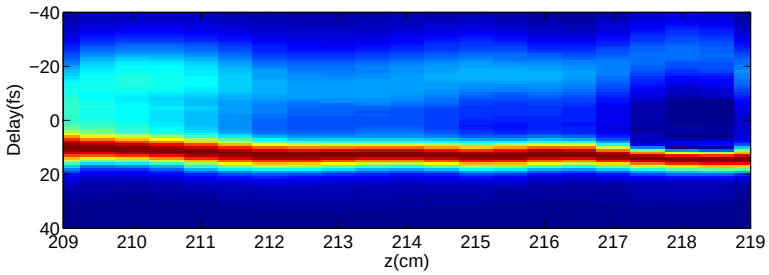

Figure 4: Experimental data for the evolution of the filamentary pulse retrieved with the setup of Ref. [20]

Third, self-steepening continuously shifts the intense trailing pulse towards positive delay, while the weak leading pulse accelerates towards negative delays. This is a consequence of the spectral redshift suffered by the leading pulse and the corresponding increase of its group velocity. Note that a crucial technical detail of our measurement was neglected in our theoretical discussion. In the experiment, two laser-drilled pinholes were employed, separated by a distance of approximately 1cm. While the first pinhole had a rather large diameter of $d = 500\,\mu$m due to additional laser ablation induced by the argon plasma, the gas pressure at the second pinhole releasing the pulses into the vacuum was significantly reduced, leading to an absence of argon plasma and a considerably smaller pinhole size of $d = 150\,\mu$m, as already confirmed in [20]. Here, using our propagation model we checked that the first, large pinhole has a minor impact on the pulse evolution, and our theoretical considerations confirmed that the small size of the second pinhole was crucial for an accurate reconstruction of on-axis pulse shapes in the filament. With respect to the above discussion, releasing the beam into the vacuum through a sequence of two pinholes therefore guarantees an undistorted reconstruction of on-axis pulse shapes in the filament and enables us to accurately monitor the process of filamentary self-compression into the few-cycle regime. Indeed, our measurements allowed the reconstruction of $5\,$fs pulses, as short as two optical cycles at the driving frequency of $385\,$THz.

5 Conclusions

In summary, we have shown that even vacuum propagation of filamentary pulses towards the detector is prone to completely obscure the on-axis near field evolution in the filament, leaving no signature of pulse self-compression or the generation of few-cycle pulses. This may explain why many groups were unable to report evidence of real self-compression and instead resorted to dispersion management techniques for pulse recompression [25]. Furthermore, it was theoretically demonstrated that the setup of [20], which involves differential pumping and extracting the filament pulse into the vacuum through a small self-induced pinhole, is in principle suitable for reconstructing on-axis pulse profiles directly in the filament.

Financial support by the Deutsche Forschungsgemeinschaft (Grant STE 762-9) is gratefully acknowledged.

References

[1] V. P. Kandidov, S. A. Shlenov, and O. G. Kosareva, Quantum Electronics **39**, 205 (2009).

[2] T. Brabec and F. Krausz, Rev. Mod. Phys. **72**, 545 (2000).

[3] A. Braun, G. Korn, X. Liu, D. Du, J. Squier, and G. Mourou, Opt. Lett. **20**, 73 (1995).

[4] M. Mlejnek, E. M. Wright, and J. V. Moloney, Opt. Lett. **23**, 382 (1998).

[5] C. Brée, A. Demircan, S. Skupin, L. Bergé, and G. Steinmeyer, Opt. Express **17**, 16429 (2009).

[6] G. Stibenz, N. Zhavoronkov, and G. Steinmeyer, Opt. Lett. **31**, 274 (2006).

[7] V. Loriot, E. Hertz, O. Faucher, and B. Lavorel, Opt. Express **17** 13429 (2009).

[8] M. Kolesik, E. M. Wright, and J. V. Moloney, Opt. Lett. **35**, 2550 (2010).

[9] C. Brée, A. Demircan, and G. Steinmeyer, Phys. Rev. Lett. **106**, 183902 (2011).

[10] O. Kosareva *et al.*, Opt. Lett. **36**, 1035 (2011).

[11] M. Kolesik, D. Mirell, J. C. Diels, and J. V. Moloney, Opt. Lett. **35**, 3685 (2010).

[12] P. Béjot *et al.*, Phys. Rev. Lett. **104**, 103903 (2010).

[13] J. Odhner and R. J. Levis, Opt. Lett. **37**, 1775 (2012).

[14] C. Iaconis and I. A. Walmsley, Opt. Lett. **23**, 792 (1998).

[15] R. Trebino *et al.*, Rev. Sci. Instrum. **68**, 3277(1997).

[16] L. Bergé, S. Skupin, and G. Steinmeyer, Phys. Rev. Lett. **101**, 213901 (2008).

[17] L. Bergé, S. Skupin, and G. Steinmeyer, Phys. Rev. A **79**, 033838 (2009).

[18] C. Brée, A. Demircan, J. Bethge, E. T. J. Nibbering, S. Skupin, L. Bergé, and G. Steinmeyer, Phys. Rev. A **83**, 043803 (2011).

[19] S. Champeaux and L. Bergé, Phys. Rev. E **71**, 046604(2005).

[20] M. Kretschmar *et al.*, Optics Express **22**, 22905(2014).

[21] A. Zaïr, A. Guandalini, F. Schapper, M. Holler, J. Biegert, L. Gallmann, A. Couairon, M. Franco, A. Mysyrowicz, and U. Keller, Opt. Express, **15**, 5394 (2007).

[22] L. Berge, S. Skupin, R. Nuter, J. Kasparian, and J. P. Wolf, Rep. Prog. Phys. **70**, 1633 (2007).

[23] A. Dalgarno and A. E. Kingston, Proc. Roy. Soc. A **259** (424), 1960.

[24] A. M. Perelomov, V. S. Popov, and M. V. Terent'ev, Sov. Phys. JETP **23** 924 (1966).

[25] A. Mysyrowitz, A. Couairon, and U. Keller, New J. Phys. **10**, 025023 (2008).